

Project: “Nanostructured Silicon-Based Tandem Solar Cells”
Institution: University of New South Wales, Sydney, Australia

Abstract

The aim of the project is the development of a potentially “game-changing” photovoltaic technology by innovative exploitation a new technology combining low-cost polycrystalline silicon thin-films with higher bandgap material synthesized using silicon quantum dots in a matrix of silicon oxide, nitride, or carbide to produce 2- or 3-cell tandem stacks, based on rugged silicon and some of its most stable and durable compounds. The approach offers a significant jump in efficiency without adding appreciably to large-volume manufacturing costs per unit, resulting in a corresponding decrease in installed system costs.

In the past year the project has continued to characterise these Si QDs in SiO₂ and developed further the successful transition to a Si₃N₄ matrix in which greater inter-quantum dot electrical mobility is expected and demonstrated because of the lower matrix barrier height. In addition a transition of the technology to a SiC matrix has been successfully initiated, because of its even lower barrier height. Furthermore the technology is also being transferred to Sn (tin) QDs in a SiO₂ matrix. This allows lower processing temperatures and also potentially an effective band gap *below* that of silicon – advantageous for tandem cell elements *underneath* a bulk-Si cell.

Characterisation of these nanostructures (typically the self-assembled QDs are only 4nm in diameter) is challenging. A combination of techniques is used and a few new ones have been developed. These include high resolution TEM, XRD and Raman for physical characterisation; photoluminescence for optical; and high resolution conductivity and capacitance techniques for electrical. Results from these demonstrate the presence of QDs, with a controllable size and size uniformity; optical evidence for confined energy levels and increased effective band gaps; and conductivity in a QD superlattice which increases as the matrix is changed from oxide to nitride.

Work on the project is now moving onto devices, both homo- and hetero-junction using these Si and Sn nanostructure materials. This will be developed further to include single junction and tandem junction devices in the next stage of the project.

Administration

Personnel

[All personnel are members of the ARC Photovoltaics Centre of Excellence, supported by the Australian Research Council.]

Principal Investigators:

Prof. Martin A. Green – Research Director, Centre of Excellence (CoE)

Dr. Gavin Conibeer – Deputy Director – Third Generation Strand, CoE

Investigators:

Dr. Dirk König – Characterisation/Modeling Strand Leader, GCEP, CoE

Dr. Eun-Chel Cho – Processing/Fabrication Strand Leader, GCEP, CoE

Dr. Tom Puzzer – Professional Officer, GCEP, CoE (part time)
Ms. Yidan Huang – Professional Officer, GCEP, CoE
Dr. Shujuan Huang – Postdoctoral Fellow, GCEP, CoE
Dr. Dengyuan Song – Postdoctoral Fellow, GCEP, CoE
Dr. Ivan Perez-Wurfl – Postdoctoral Fellow, GCEP, CoE
Dr. Thorsten Trupke – Associate Professor, GCEP, CoE (part time)
Dr. Chu-Wei Jiang – Postdoctoral Fellow, GCEP, CoE (part time)
Dr. Patrick Campbell – Research Fellow, GCEP, CoE (part time)
Mr. Edwin Pink – Research Associate, GCEP, CoE (part time)

Postgraduate Students, CoE:

Mr. Young Cho (PhD)
Ms. Thipwan Fangsuwannarak (PhD)
Mr. Christopher Flynn (PhD)
Ms. Xiaojing ‘Jeana’ Hao (PhD)
Mr. Sangwook Park (PhD)
Mr. Edwin Pink (PhD)
Mr. Giuseppe Scardera (PhD)
Ms. (MPhil)

Staff changes

Mar 2006 – Chris Flynn started as a PhD student
June 2006 – Xiaojing Hao started as a PhD student
June 2006 – Sangwook Park started as a PhD student
Aug 2006 – Chu-Wei Jiang – Postdoctoral Fellow - left
Dec 2006 – Ivan Perez-Wurfl started as a Postdoctoral Fellow
Feb 2007 – Lara Treiber started as Masters student
March 2007 – Edwin Pink transferred from Research Assoc. to PhD student
April 2007 – Thipwan Fangsuwannarak graduated PhD and left

Equipment (mainly funded on other projects)

Mar-Aug 2006– Multitarget sputtering machine installed and commissioned
Sept-Dec 2006– Dual E-beam specified and ordered, delivery is scheduled for May07
June-Dec 2006– Computer cluster – Gaussian: ordered, delivered - operational Feb07

Organisation

The project is split into four strands, Modelling, Processing, Characterisation and Device Fabrication. In last year’s annual report (which reported on only three months of full time work) the Modelling and Characterisation strands were combined and the Device strand was not yet initiated. In the last year there has been significant development of the first two of these into discrete strands (although still under the same manager). Also initial test devices fabricated such that Device Fabrication will soon form a separate strand.

1 Introduction

The aim of the project is the development of a potentially “game-changing” photovoltaic technology (*today’s highest efficiencies at tomorrow’s lowest projected costs*) by innovative exploitation of past silicon solar cell developments at the University of New South Wales (UNSW). The new technology combines low-cost polycrystalline silicon thin-films with higher bandgap material synthesized using silicon quantum dots in a matrix of silicon oxide, nitride, or carbide to produce 2- or 3-cell tandem stacks, based entirely on rugged silicon and some of its most stable and durable compounds. The approach offers a significant jump in efficiency without adding appreciably to large-volume manufacturing costs per unit, resulting in a corresponding decrease in installed system costs. The aim is to accelerate the development of this technology, to position it for industrial investment in its commercialization by the project’s conclusion (end August 2008).

2 Background (with reference to other work in the field)

Fabrication of silicon nanocrystals embedded in a dielectric matrix has attracted considerable interest in silicon optoelectronics [1,2,3] and in third generation photovoltaics [4,5]. When silicon nanocrystals are made very small ($< \sim 7$ nm in diameter), they behave as quantum dots (QDs) due to three-dimensional confinement of carriers [4]. Quantum confinement causes material’s effective bandgap to increase. In indirect band-gap semiconductors the optical transitions are allowed only if phonons are absorbed or emitted to conserve the crystal momentum. The localisation of electrons and holes inside a QD leads to reflections or folding of phonons in k -space. This relaxes the k -conservation requirement and creates a quasi-direct bandgap. Our measurements of photoluminescence (PL) from Si QDs in silicon oxide has confirmed that we get a 1.7 eV lowest energy transition from 2 nm quantum dots; effectively a 1.7eV bandgap [6]. They also show that there is a large increase in PL intensity as the QD size decreases, which is consistent with the increase in radiative efficiency with the onset of pseudo-direct band gap behaviour.

For photovoltaic applications, nanocrystal materials may allow the fabrication of higher bandgap solar cells that can be used as tandem cell elements on top of normal Si cells [4,5]. For an AM1.5 solar spectrum the optimal bandgap of the top cell required to maximize conversion efficiency is ~ 1.7 to 1.8 eV for a 2-cell tandem with a Si bottom cell [7]. To date, considerable work has been done on the growth and characterization of Si nanocrystals embedded in oxide [8,9] and nitride [10,11] dielectric matrices. However, little has been reported on the experimental properties of Si nanocrystals embedded in SiC matrix [12].

Another requirement for a tandem cell element is the presence of some form of junction for carrier separation. The impurities in bulk crystalline silicon play an important role in a semiconductor device. Dopants such as phosphorous and boron alter the conductivity of bulk Si by several orders of magnitude. There are several questions about the impurity doping in a low-dimensional structure [13]. Important questions arise as to whether the dopants will continue to play a role similar to that in bulk semiconductors, or whether alternative methods of work function control will be required. It is not clear at present whether or not the doping of Si nanocrystals

provides the generation of free charge carriers [14]. The junction can either be a grown or a diffused p–n junction or a p–i–n junction with the superlattice as the i-region. The latter requires careful control of the work functions (and therefore doping) of the p and n-regions but also means that it is not essential for the superlattice itself to be doped.

In our work we have also observed that the photoluminescence peaks from Si QDs in nitride are more blue-shifted than that of Si QD in oxide. Figure 1 shows the results of other workers for PL peak energies from Si QD dispersed in oxide [15,16,17] and nitride [10,18]. PL peak energies of Si QDs in oxide are less than 2.0 eV while Si QDs in nitride have peak energies less than 3.0 eV. Puzder *et al.* [19] have explained that the main reason for the PL peak energy reduction in oxide matrix is the distortion of the local sp^3 network by double-bonded oxygen. However, Yang *et al.* [20] claimed that the reason for the stronger blue-shift in nitride is better passivation of Si QDs by nitrogen atoms eliminating the strain at the Si/Si₃N₄ interface nearly completely.

Our PL results from the Si precipitation are in quite good agreement with the results from other authors [15,16,17,18,10] (see Figure 1) and in general are consistent with the results from modelling which indicate an effect of the matrix on confined energy levels. Our own work in this area using ab-initio modelling (HF-DF with Gaussian software) shows a decrease in confined energy level, for a given size of Si nanocrystal, on going from nanocrystals terminated by H (equivalent to vacuum) to those terminated with –NH₂ groups (\equiv to nitride) to those with –OH groups (\equiv oxide) due to the differing lowest local energy states of surface Si atoms [21]. Further modelling is reported in Section 3.2 below.

The modeling of Si QDs in the DFT regime is a frequent topic in the literature, though the Si approximants are usually terminated by hydrogen (H) atoms [22]. Some authors investigated the effect of oxygen (O) double- and bridge-bonds to the Si core of the otherwise H-terminated approximants [23,24] or the termination of the Si core with Alkyl (C_xH_y) groups [25]. To the best of our knowledge our method to terminate all Si surface bonds with functional groups of the respective dielectric matrix (-OH, -NH₂, -CH₃) with the high accuracy B3LYP hybrid functional and a Gaussian orbital basis set was not mentioned in the literature so far. There are no reports in the literature about Amino-group (-NH₂) terminated Si QDs; this appears to be a new approach, see Section 3.2.

Clear evidence of confinement in Si quantum dots in carbide was hard to obtain, probably due to many surface and defect states which dominate the photoluminescence process [26]. An observation of clear quantum confinement in the Si QDs dispersed in SiC matrix is also very challenging since usually meta-stable alloy films relax by diffusion and/or misfit dislocation formation to reduce chemical modulation and strain. The initial PL result shows two peaks corresponding to the Si quantum dots and SiC matrix. Clarification of quantum confinement in Si QDs in a SiC matrix is the subject of on-going work. It is likely that the mechanism of precipitation of excess Si atoms to nucleating sites in Si rich SiC is a less active process than in nitride or oxide. This would be because the difference in Si-Si and Si-C lattice spacing is less than in the nitride and oxide. Also because SiC is an isoelectronic covalently bonded material, as is Si, so there is a much smaller tendency for segregation of Si than in oxide or nitride matrixes.

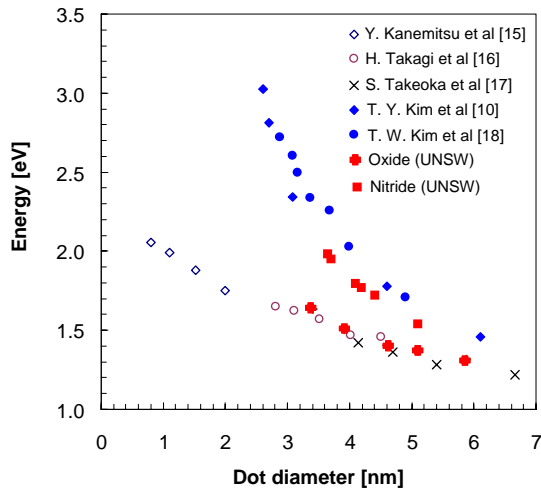


Figure 1: Experimental energy gaps of three-dimensionally confined Si nanocrystals in SiO₂ and SiN_x (300°K) from several authors [15,16,17,10,18].

3 Progress May 2006 – April 2007

3.1 The “all-Si” Tandem cell

Silicon is a benign readily available material, which is widely used for solar cell fabrication. Silicon also has a bandgap which is close to optimal not only for a standard, single p-n junction cell (a little too low) but also for the bottom cell in a 2-cell or even a 3-cell tandem stack (a little too high). The radiative efficiency limit for a single junction silicon cell is 29%. This increases to 42.5% and 47.5% for 2-cell and 3-cell tandem stacks respectively. The optimal bandgap of the top cell is 1.7 eV ~ 1.8 eV for a 2-cell tandem with a Si bottom cell and 1.5 eV and 2.0 eV for the middle and upper cells for a 3-cell tandem [27].

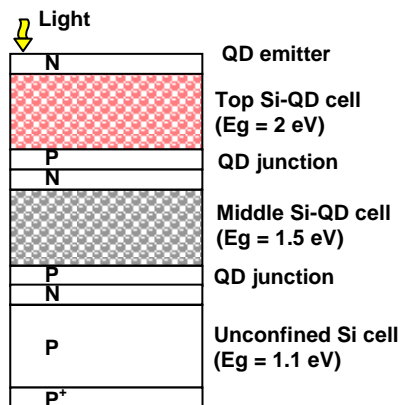


Figure 2: Schematic of “all-silicon” tandem solar cell.

Our approach is to produce a material with an engineered band gap using small nanocrystals of Si embedded in a silicon dielectric matrix, with the nanocrystal size approaching the Bohr radius. The resultant quantum confined energy levels will give an increase in the effective band gap of the nanostructure as compared to bulk Si. By restricting at least one dimension of silicon to the Bohr radius of the bulk crystalline

silicon (5 nm or less), quantum confinement cause its effective bandgap to increase. Our early experiments involved carefully thinning the thin silicon layer (50 nm thick) in commercially available silicon-on-insulator wafers [28] and showed clear PL evidence for a quantum-confined bandgap increase up to 1.7 eV for layers about 1 nm thick. Also with an increased strength of optical processes due to the localisation of electron-hole pairs – which is important for solar cell applications. This work was developed further by constraining Si in all three dimensions in nanocrystals to achieve a much stronger quantum confinement effect.

We are now investigating Si QDs in SiO₂ and analogues in other silicon dielectrics such as silicon nitride and silicon carbide, and also other group IV analogues such as Sn QDs in SiO₂.

We have adopted a threefold strategy for this work. Firstly we are model the materials and structures with respect to their quantum confined properties, doping potentials and suitability as wide band gap photovoltaic materials. We then try to fabricate these nano-structure materials using thin film deposition techniques, including: sputtering, PECVD and e-beam evaporation. These are then characterised with respect to their physical, optical and electronic properties with a high spatial resolution and sensitivity. Results from these are modelled interpretively before feeding into the next stage of modelling, fabrication and characterisation.

Theory of Si QD superlattice formation

Transport properties are expected to depend on the matrix in which the silicon quantum dots are embedded. As shown in Figure 3, different matrices produce different transport barriers between the Si dot and the matrix, with tunnelling probability heavily dependent on the height of this barrier. Si₃N₄ and SiC give lower barriers than SiO₂ allowing larger dot spacing for a given tunnelling current.

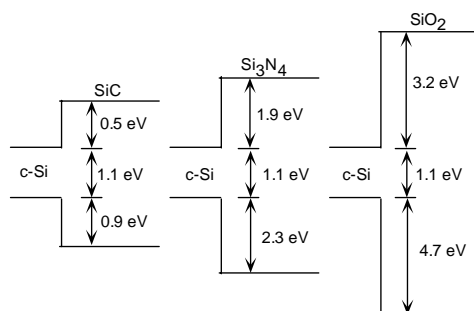


Figure 3: Bulk band alignments between crystalline silicon and its carbide, nitride and oxide.

The wave function of an electron confined to a spherical dot penetrates into the surrounding material, decreasing exponentially into the barrier. The slope of this exponential decay and hence the barrier to tunnelling between quantum dots is reduced for a lower barrier height material. This is because - from transmission/reflection probability - the tunnelling probability T_e through a square potential well depends exponentially on three parameters, the barrier width d = the spacing between quantum dots; the square root of the barrier height seen by the electron ($\Delta E^{1/2}$ the energy difference between the CB edge of the matrix and the confined energy level of the quantum dots = $(E_c - E_n)^{1/2}$); and the square root of the

effective mass $(m^*)^{1/2}$ of the electron within the barrier. This gives approximately, (e.g. [29] p244):

$$T_e \approx 16 \exp \left\{ -d \sqrt{\frac{8m^*}{\hbar^2} \Delta E} \right\} \quad (2)$$

Hence the important parameter in determining the degree of interaction between quantum dots is $m^* \Delta E d^2$. As barrier height decreases the barrier thickness for a given probability increases, thus requiring a lower dot density for a given conductivity or higher conductivity for a given dot density. As the dot size decreases ΔE also decreases, thus increasing T_e and enhancing the effect further for smaller quantum dots [29]. The results suggest that dots in a SiO₂ matrix would have to be separated by no more than 1-2 nm of matrix, while they could be separated by more than 4 nm of SiC. Fluctuations in spacing and size of the dots can be investigated using similar calculations. It is also found that the calculated Bloch mobilities do not depend strongly on variations in the dot spacing but do depend strongly on dot size within the QD material [30].

Hence, transport between dots can be significantly increased by using alternative matrices with a lower barrier height, ΔE . The spacing of dots would have to be closest in the oxide, nitride and carbide, in that order. Similar deposition and quantum dot precipitation approaches should work for all.

3.2 Modelling

Ab-initio modeling using Density Functional – Hartree-Fock (DF-HF) techniques

Hardware

At the end of 2006 a Beowulf-type Linux cluster was commissioned at the ARC-PV-CoE. It consists of ten computer nodes and one link node each having two 64bit AMD Opteron Dual Core CPUs, 4 GB RAM and two 180 GB HDDs which are run in RAID0 mode for maximum 64bit data bandwidth. The cumulative 44 Opteron cores enable the cluster to have an estimated peak computing performance of 240 GFLOP/s.

Software

As software for the DF-HF computations we used the parallel implementation of the commercial simulation package Gaussian03 [31]. Gaussian03 is a DF-HF based ab-initio program for calculating basic thermodynamic, electronic and phononic properties of approximants consisting of up to a few hundred atoms in the quantum mechanical regime, and, to some extent, in the molecular dynamic regime. Gaussian03 computes the molecular orbitals (MOs) of the atomic cluster in spatial space and thus delivers a spatial picture of respective states of the approximant as a function of energy. Thermodynamic optimisations (variational principle) deliver the thermally relaxed configuration of the approximant which is the starting point for calculating its electronic structure, delivering the MO energies from which we can compute the DOS(E). An 6-31G(d) MO basis set and the B3LYP hybrid functional were used for the electronic structure computations as a good compromise between MO sets with the highest accuracy like 6-311+G(2df) and a feasible computational effort.

Results

One fundamental scientific issue is the question to what extent and in what way the interface of an Si QD controls its electronic structure. Instead of embedding an Si QD into an SiO_2 or Si_3N_4 matrix compromised by terminating the Si QD with the respective functional groups (-OH, $-\text{NH}_2$) in analogy to a first next neighbour tight binding approximation (1nn-TBA). This decreased the computation effort considerably and enabled us to go for bigger Si cores for the approximants.

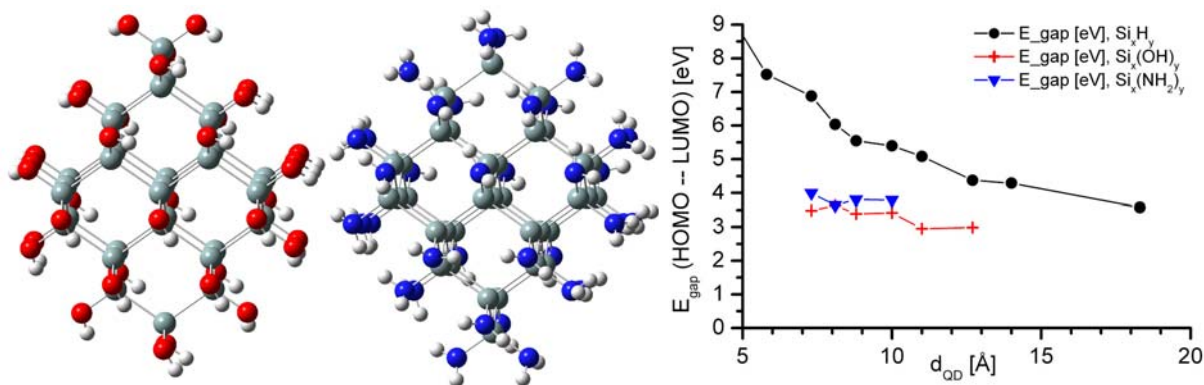


Figure 4: $\text{Si}_{35}(\text{OH})_{36}$ [left] and $\text{Si}_{35}(\text{NH}_2)_{36}$ [middle] approximants before optimization. The Si core volume corresponds to $d_{\text{QD}} = 11 \text{ \AA}$. The right graph shows the highest occupied MO (HOMO) – lowest unoccupied MO (LUMO) gaps of -H, -OH and $-\text{NH}_2$ – terminated Si cores as $f(d_{\text{QD}})$.

In contrast to a potentially co-valent termination of the Si cores with H atoms the OH- and NH_2 - terminated Si cores show a significantly lowered band gap as well as a dramatically decreased gradient $\Delta E_{\text{gap}}/\Delta d_{\text{QD}}$. It appears that the anionicity of the interface counteracts the quantum confinement in the Si core. Consequently, smaller Si QDs may be required for realising an optical absorption at a desired effective band gap. On the other hand, the effective band gap seems to be less vulnerable to deviations from a nominal QD size due to the decreased gradient $\Delta E_{\text{gap}}/\Delta d_{\text{QD}}$ which may increase the process tolerance for QD array preparation. The band gaps are maximum values for realistic Si QDs since the computed approximants are free of any defects and embedded in vacuum.

Another aspect is the investigation of dielectric matrices like SiO_2 , Si_3N_4 or SiC. Typical defects like Si dangling bonds (DBs) and their impact on the electronic structure are of vital interest.

From Figure 5 it can be seen that an Si-DB introduces two defect levels within the band gap of which one – MO254 β – is near midgap. This could be a major obstacle to very high photo luminescence (PL) radiation efficiencies. It is also remarkable to see the shift of the valence band edge to higher energies as a result of the Si-DB.

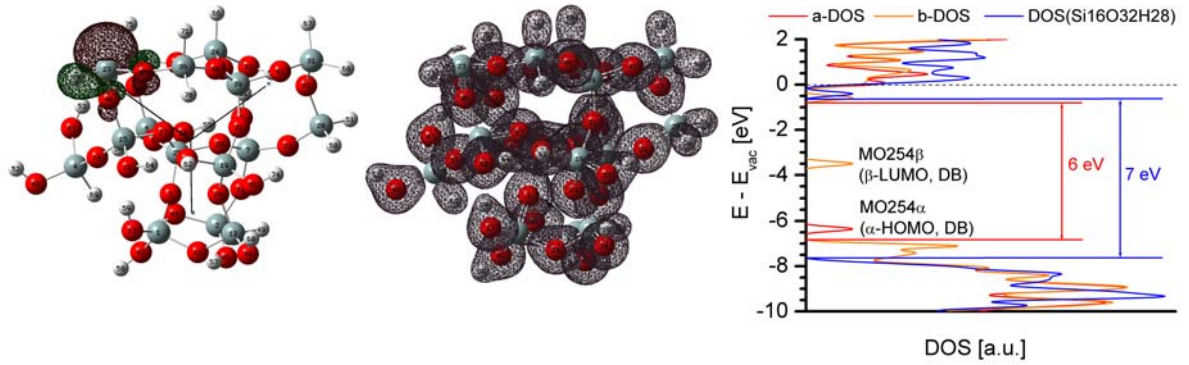


Figure 5: SiO_2 approximant with a Si-DB ($\text{Si}_{16}\text{O}_{32}\text{H}_{27}$): α -HOMO being located at the Si-DB [left]; the corresponding β -LUMO has the same MO distribution but opposite sign of the wave function (spin). Electronic charge density of the $\text{Si}_{16}\text{O}_{32}\text{H}_{27}$ approximant [middle]. The Si-DB with the charge density of its α -HOMO is shown by an arrow. DOS of the $\text{Si}_{16}\text{O}_{32}\text{H}_{27}$ approximant compared with the one of a defect free approximant ($\text{Si}_{16}\text{O}_{32}\text{H}_{28}$) [right]. The α - and β - DOS account for electrons with opposite spins. A gaussian broadening of the MOs of 0.1 eV was assumed.

Starting from the approximants consisting of Si cores terminated with functional groups a Si-QD with $d_{\text{QD}} = 11 \text{ \AA}$ (Si_{35}) was embedded into 1.5 mono layers (MLs) of 3C-SiC. The MLs of the dielectric matrix enables us to investigate defects in the dielectric in the immediate proximity to the Si-QD.

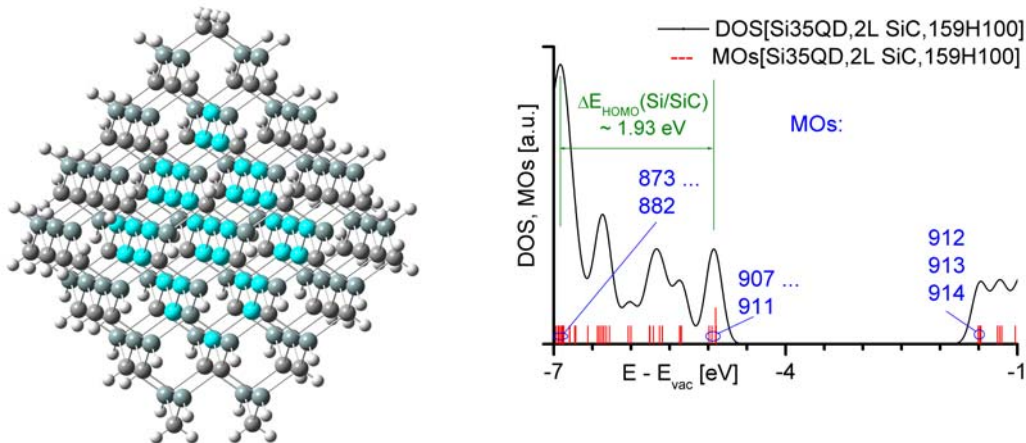


Figure 6: Si_{35} core embedded in 1.5 MLs of 3C-SiC ($\text{Si}_{35}\text{-Si}_{60}\text{C}_{64}\text{H}_{100}$) [left]. The Si core is highlighted in blue. MOs and DOS of the $\text{Si}_{35}\text{-Si}_{60}\text{C}_{64}\text{H}_{100}$ approximant [right]. The DOS was calculated by gaussian broadening of the MOs by 0.1 eV. For the MO numbers see Figure 5.

The resulting approximant is shown in Figure 6 [left]. The DOS shows a clear distinction between the HOMO being confined to the Si core (MO 907 to 911) and highest occupied MO within the SiC (MO 873 to 882), compare Figure 6 [right] and Figure 5 [left, middle]. There is an energetic difference of 1.93 eV which can be interpreted as the valence band offset between the Si core and the SiC shell, being enhanced due to quantum confinement within the complete approximant. An assignment of the respective MOs to the conduction band edge of SiC is not possible as these MOs are not clearly confined to the Si core nor to the SiC shell. This indicates that the spatial transition region of the conduction band edge is significantly

more spread out than the one of the valence band edge, or in other words: The electronic interface is wider for conduction band states, while for valence band states the transition is rather abrupt. This may have a noticeable impact on carrier transport. Namely, the tunnelling of electrons may be enhanced over holes for thin SiC barriers.

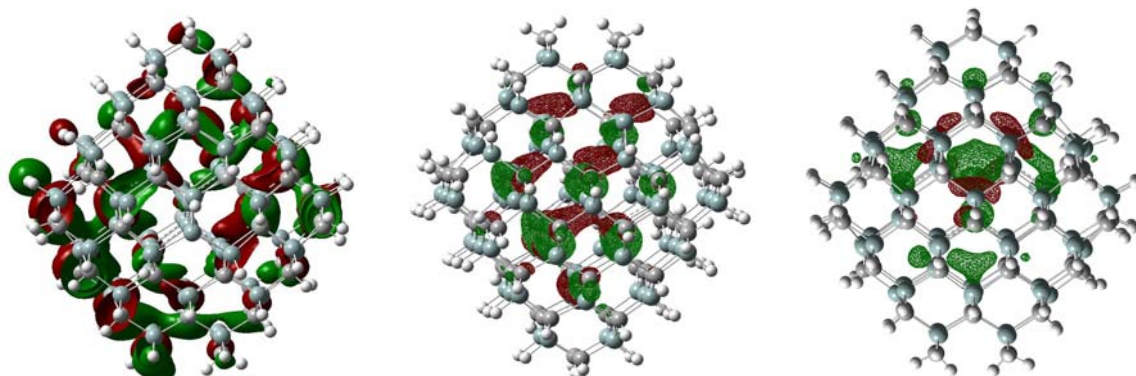


Figure 7: Si₃₅ core embedded in 1.5 MLs of 3C-SiC (Si₃₅-Si₆₀C₆₄H₁₀₀): Sum of the MOs 873 to 882 [left; iso-surfaces cut at the symmetry plane], of the MOs 907 to 911 [middle] and 912 to 914 [right]

Further computations to obtain a more detailed picture are under way.

Simulation of TEM imaging and artefacts

Nanoscale structured materials and systems play a central role in the development of Third Generation solar cell structures. The physical parameters determining the ultimate nanoparticle properties are the elemental composition, size, external shape and internal structures. Characterising these materials and their nanostructures is an essential part of the research project. Although other techniques such as X-ray diffraction and selected-area electron diffraction, can provide accurate structural information (averaged over the excited sample volume), they are incapable of providing information on the structure of individual nanoparticles. The information contained in the diffraction pattern, however, extends much further in reciprocal space than is accessible to HRTEM. Since the various types of microscope aberrations do not influence electron diffraction, high resolution electron diffraction data can be obtained without imaging artefacts.

Despite the difficulties involved with HRTEM, it remains the most powerful technique to examine these materials at sub-nanometre resolution. It is important to remember, however, that the image formation system of the TEM is not perfect. The contrast transfer function (see Figure 8) contains zeros and inversions meaning that some spatial frequencies present in the sample are not observed in the images and other spatial frequencies are imaged with reversed contrast. Therefore, there is a problem with unambiguous interpretation of individual high-resolution images and only under well-defined conditions may high-resolution images be naively interpreted in terms of the projected potential of the atomic columns aligned along the beam direction.

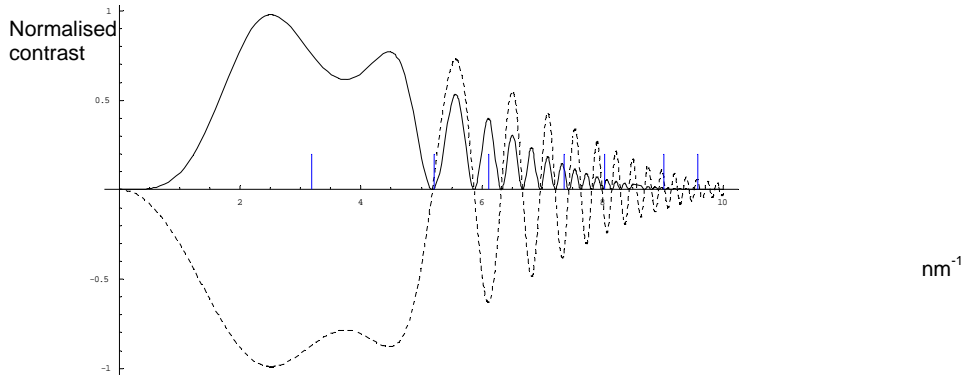


Figure 8: Contrast transfer function (CTF) at the Scherzer defocus (maximum passband). [CTF – dashed line; CTF^2 – solid line.] Si low index planes are indicated by the blue vertical lines. The Si(111) is in the main passband; Si(220) is at a point of zero contrast; Si(311) is in a passband with a positive contrast. [32]

In order to model which nanocrystals are likely to be observable above the noise level in HRTEM images, a 3nm QD is modelled in a range of low index plane configurations, see Figure 9.

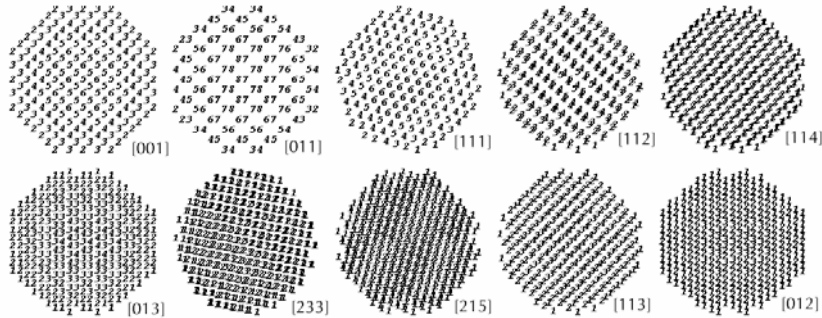


Figure 9: Simulated 3nm Si spheres are rotated to low-index zone axes and embedded in a 3nm thick white-noise silica layer (same nominal density as bulk SiO_2). The numerals indicate the number of atoms in projection for each atomic column in the particle. [N.B. There is no intentional particle faceting in this model – (just bond-length + truncation).] [33]

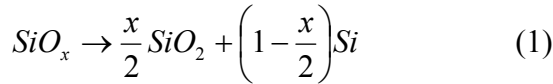
The numbers on each nanocrystal indicate the number of atoms in projection for each atomic column in the particle. If this number exceeds the average number of atoms in the amorphous phase then contrast is expected. The modelling proceeds by embedding the simulated nanocrystals in an amorphous background. To model the latter a simple model based on determining the smallest cell that contains a SiO_2 molecule is used and randomly placing one Si and two O atoms in this cell. This gives the number of projected atoms per square \AA . For a 3nm thick SiO_2 layer in this model: the mean number of Si and O atoms are 4.3 atoms/\AA^2 and 8.5 atoms/\AA^2 , respectively. This results in a random arrangement of “columns” of atoms in the amorphous phase with the number of atoms varying from 3 to 8 atoms.

Hence only those nanocrystals with columns of 6 or more atoms would be expected to have good contrast. These are the [110] and [111] orientations. Add to this the fact that the usual mode of operation is to focus the TEM around the Scherzer defocus and it can be seen from Figure 8 that of these planes only the [111] will be in a pass band. Thus it is not surprising that one tends to only resolve [111] planes in HRTEM images. Hence this does not indicate a lack of nanocrystals with other orientations.

3.3 Fabrication of Si QD nanostructures

Commonly used thin film techniques are used for nanostructure fabrication. These include sputtering and plasma enhanced chemical vapour deposition (PECVD). The deposition is a variation of the multi-layer alternating ‘stoichiometric dielectric / Si-rich dielectric’ process described below, followed by an annealing during which Si nanocrystals precipitate. The most successful and hence most commonly used technique is sputtering, because of its large amount of control over deposition material, deposition rate and abruptness of layers. This uses a new multi-target remote plasma sputtering machine with two independent RF power supplies as well as an additional DC power supply.

RF magnetron sputtering is used to deposit alternating layers of SiO₂ and SRO of thicknesses down to 2nm. [SRO refers to Si rich oxide, formed by co-sputtering Si and SiO₂.] Deposition of multi-layers, consisting typically of 20 to 50 bi-layers, is followed by an anneal in N₂ from 1050 to 1150°C. During the anneal the excess silicon in the SRO layer precipitates to form Si nanocrystals between the stoichiometric oxide layers according to the following reaction, Eq.(1):



Experimental results have shown that the size of the QDs can be quite well controlled by selecting an appropriate thickness for the SRO layer and the density of the dots can be varied by the composition of the SRO layer. This control is possible for layer thicknesses less than about 7nm, within which Si migration to nucleating sites is dominated by a 2D rather than a 3D diffusion regime. Figure 10 shows typical transmission electron microscope (TEM) and high resolution TEM (HR-TEM) images of Si nanocrystals grown using this method. TEM evidence indicates that these nanocrystals tend to be spherical - as surface energy minimisation would dictate - and at this scale would have energy levels confined in all three dimensions and hence can be considered as quantum dots (QDs) [6]. This technique is adapted from that of Zacharias for solar cells [8].

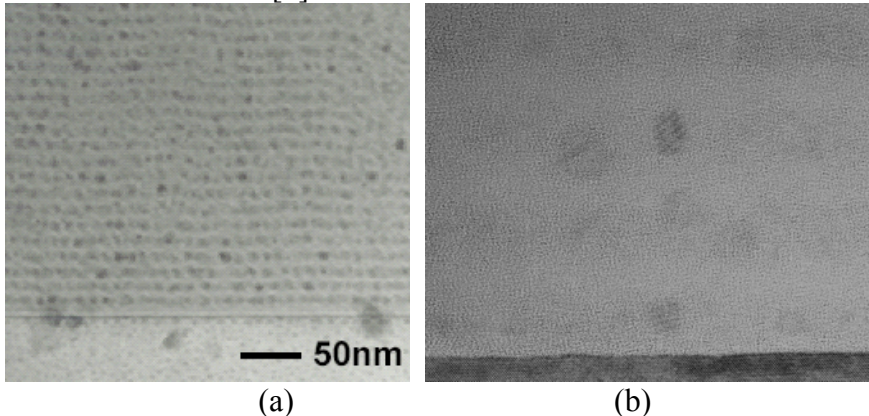


Figure 10: TEM image of Si quantum dots in a SiO₂ matrix with low magnification (a) and HRTEM image showing Si {111} lattice planes.

The main challenge for a nanostructure engineered material for a tandem cell is to achieve sufficient carrier mobility and hence a reasonable conductivity. For a

nanostructure this generally requires formation of a true superlattice with overlap of the wave function for adjacent quantum dots; which in turn requires either close spacing between QDs or low barrier height. This is discussed further in the next section.

Another requirement for a PV cell element is the presence of some form of carrier separation of photo-generated carriers. This is usually achieved with a grown or diffused p-n junction or a p-i-n junction. In our experiments, the phosphorus doping in the Si QD superlattices has been attempted using P_2O_5 co-sputtering during the deposition of silicon-rich oxide (Si and SiO_2 co-sputtering), which forms Si QDs upon high temperature post-annealing. The P concentration in the silicon-rich oxide was controlled by the deposition rate of three targets and is initially chosen to be very high – much higher than doping concentrations - in order to increase the chances of detection. Phosphorus 2p X-ray photoelectron spectroscopy (XPS) spectra show that P-O bonds (peak around 135 eV) and P-Si bonds and/or free phosphorus (peak around 129 eV) are observed from highly P-doped silicon-rich oxide (Figure 11). $SiO_{1.41}$ with 0.67 at % phosphorus shows both Si-P and O-P bonding, while silicon-rich $SiO_{0.94}$ with 0.27 at % phosphorus shows only Si-P bonding. Control of the P concentration in this way was high, in the ranges of 0.26 at% ~ 3.02 at%. The XPS results indicates that the phosphorus in silicon-rich oxide may exist in Si-P bonds inside Si QDs, however it is necessary to carry out more analytical experiments for both n-type and p-type Si QDs in different matrices.

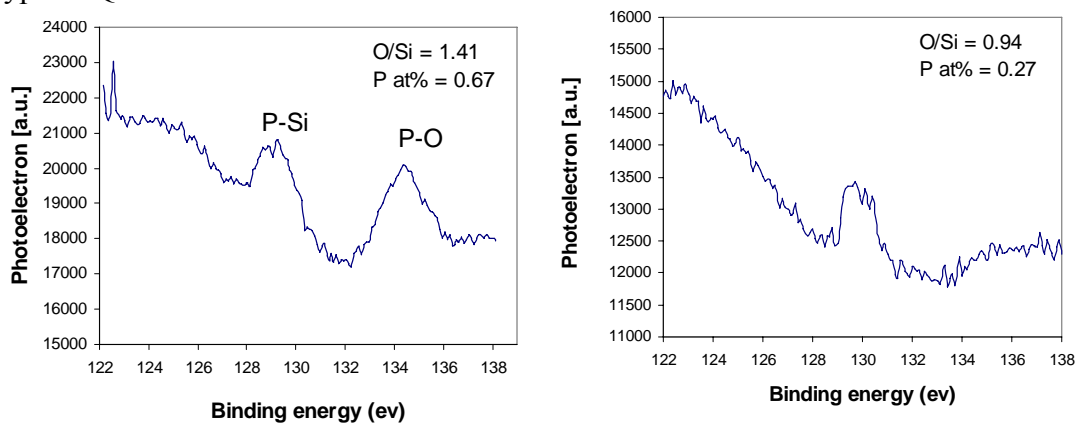


Figure 11: XPS spectra of P-Si and P-O bonding from (a) $SiO_{1.41}$ with phosphorus concentration of 0.67 at% and (b) $SiO_{0.94}$ with phosphorus concentration of 0.27 at%.

The final challenge for a tandem cell is the inter-cell connections between adjacent cells. These must connect the valence band of one cell to the conduction band of the other. This can be achieved with an interband tunnel junction or with a metallic type, defect dominated, high recombination junction. This could be achieved with a quantum dot material, with very small QDs, or a nanocrystalline Si based material.

Si quantum dots in a silicon nitride matrix

For the reasons stated above of increased tunneling probability in matrices other than SiO_2 , we have explored transferring the technology of Si QDs in SiO_2 to the growth of Si nanocrystals in silicon nitride by both sputtering and PECVD [11]. For sputtering, growth parameters are very similar to the oxide. In addition, two separate

PECVD systems – a remote plasma and a parallel capacitor machine - have been used for the growth of Si nanocrystals by depositing alternate Si rich and stoichiometric nitride layers. Annealing is carried out again at 1100°C but with a pre-annealing at 500°C to drive off hydrogen incorporated from the PECVD process. Again HRTEM images showing even clearer nanocrystals have been obtained. To the best of our knowledge this is the first time layered Si QDs in nitride [11].

We have now also extended the layered Si QDs in nitride technology to gas-phase *in situ* deposition. Figure 12 shows *in situ* Si QD dispersed in a nitride matrix. A stoichiometric Si₃N₄ layer and an *in situ* Si QD layer are alternately deposited on a Si substrate. This technique allows QDs to form during deposition without the need for a subsequent anneal. We are actively studying this technique because it is a low temperature process and potentially lends itself to doping of Si QDs.

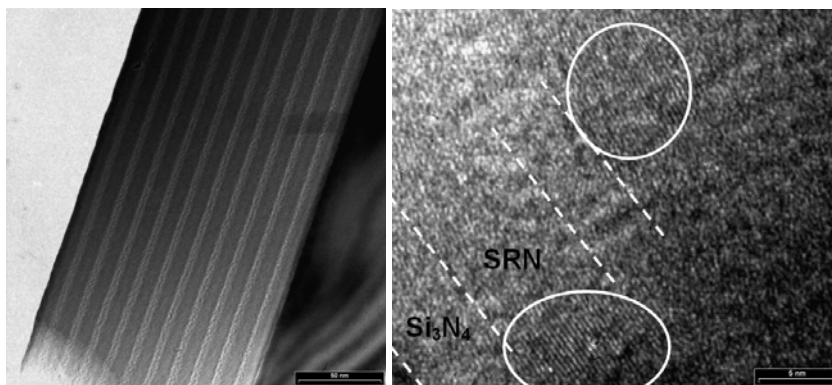
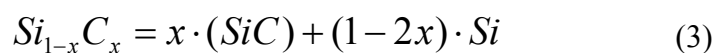


Figure 12: Gas phase *in situ* Si QDs dispersed in a Si₃N₄ matrix: (a) low magnification TEM and (b) high resolution TEM.

Si QDs in silicon carbide

For a similar reason we are also investigating transfer of the Si QD technology to a SiC matrix. SiC nanocrystals of a few nm diameter in a SiO₂ matrix were produced by silicon and carbon implantation into thermal oxide [26]. However, to our knowledge, little has been reported on the experimental properties of Si QDs embedded in a SiC matrix.

A Si-rich amorphous silicon carbide precursor layer can be achieved by control of the sputtering parameters of Si and carbon containing targets (e.g. pure carbon, silicon carbide, boron carbide etc). One way to fabricate Si-rich silicon carbide is co-sputtering from silicon and carbon containing targets. Alternatively small chips of carbon attached to a silicon target can produce a Si-rich silicon carbide precursor layer. A high temperature anneal (800-1200°C in an inert gas or in vacuum) of a silicon rich carbide precursor layer precipitates Si and/or SiC nanocrystals depending on its chemical composition as follows:



Raman, TEM and XRD spectra for a silicon-rich Si_{0.75}C_{0.25} precursor layer grown on a quartz substrate with subsequent annealing are shown in Figure 13. There is clear

evidence for the formation of nano-crystalline Si at an anneal temperature greater than 1000°C. This is shown in the Raman peak at $\sim 508 \text{ cm}^{-1}$ (red shifted from 520 cm^{-1} due to a nanocrystalline folded Brillouin zone dispersion in k-space); TEM lattice fringe spacing consistent with $\{111\}$ Si planes; and XRD peaks at $2\theta = 28.4^\circ$ with peak broadening indicating nanocrystal of 3-7nm (estimated using the Scherrer equation). [It should be noted that the nanocrystal size determined by TEM is, in our experience, slightly smaller than that determined by XRD.]

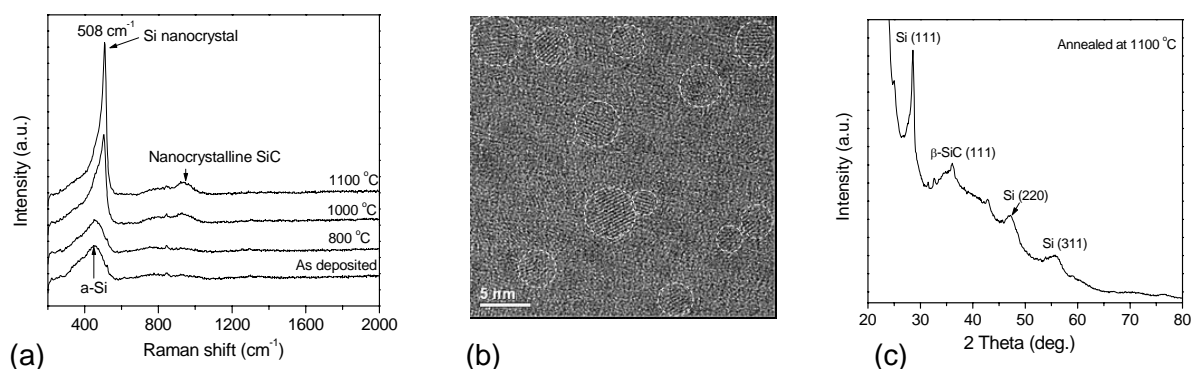


Figure 13: Silicon-rich SiC precursor layer: (a) Raman spectra for various annealing temperatures; Cross-sectional HRTEM image; and (c) X-ray diffraction.

Other Si & C concentrations were tried. As the concentration of C in SiC_x is increased to the nearly stoichiometric $\text{Si}_{0.495}\text{C}_{0.505}$, Raman evidence for the stretching vibration modes of Si-C and C-C bonds can be easily identified. With increasing annealing temperature showing increasing intensities of both TO and LO bands, indicating the formation of crystalline SiC during annealing. In addition there is a dramatic decrease in the intensity of Si-Si vibration modes indicating the formation of far fewer Si nanocrystals. There is also evidence for free carbon at $\sim 1400 \text{ cm}^{-1}$ in as-deposited film, splitting into two bands at ~ 1360 (D band) and 1590 cm^{-1} (G band) after annealing above 1000°C , indicating formation of amorphous graphitic carbon [34].

HRTEM data shows crystallites with lattice fringes corresponding to $\beta\text{-SiC } \{111\}$ planes, with a mean size in the range of 3 - 10 nm. However, in contrast to the spherical Si nanocrystals in the silicon-rich SiC precursor, SiC nanocrystals are irregular with some nanocrystals joined together to form an extended crystal. XRD results show SiC peaks for $\beta\text{-SiC } \{111\}$, $\beta\text{-SiC } \{220\}$ and $\beta\text{-SiC } \{311\}$ planes, with a very weak peak at $2\theta = 28.3^\circ$ from Si $\{111\}$ planes. A Scherrer equation estimate of SiC nanocrystal size of gives $7.3 \pm 0.4 \text{ nm}$.

The difference of nanocrystal shapes from silicon-rich SiC and near-stoichiometric SiC is due to the differing mechanisms for nanocrystal formation. For the Si rich carbide precursor, nanocrystals precipitate to nucleating sites, due to an excess of Si in the matrix. Surface energy minimisation favouring formation of spheres. For the near-stoichiometric composition, SiC nanocrystals formation does not depend on precipitation and hence random shapes occur, dependent more on local concentration variations.

For an intermediate composition ($\text{SiC}_{0.5}$ to $\text{SiC}_{0.8}$) evidence for a mixture of Si and SiC nanocrystals is observed, with estimated nanocrystal sizes from XRD around 7.5 ± 0.5 nm and 5.1 ± 0.4 nm, respectively.

Hence the best data so far for Si nanocrystals in a SiC matrix are obtained for a $\text{Si}_{0.75}\text{C}_{0.25}$ precursor composition. Optical measurements of optical band gap and absorption coefficient are being carried out on these layers and indicate an optical gap increasing from 1.4 to 1.6 to 2.0 eV for as-deposited material annealed at a T_a of 800 or 1100°C, see Figure 14.

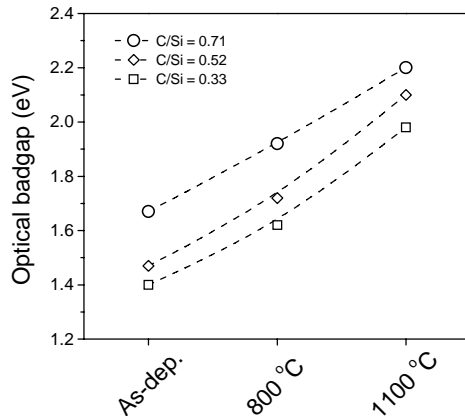


Figure 14: Effect of T_a and $R_{C/Si}$ on film optical bandgap.

A multilayer approach was also used to fabricate Si QDs in carbide in order to obtain a uniform size. A multilayer with stoichiometric SiC and silicon-rich $\text{Si}_{1-x}\text{C}_x$ precursor layer was fabricated as shown in Figure 15 and annealed at a high temperature to selectively precipitate Si nanocrystals in a carbide matrix. However, the lattice fringes in HRTEM image correspond to $\beta\text{-SiC}$ {111} crystalline planes (Figure 15(b)). One possible reason for SiC QDs instead of Si QDs is the C/Si ratio in layered structure has an increasing compared to the original design.

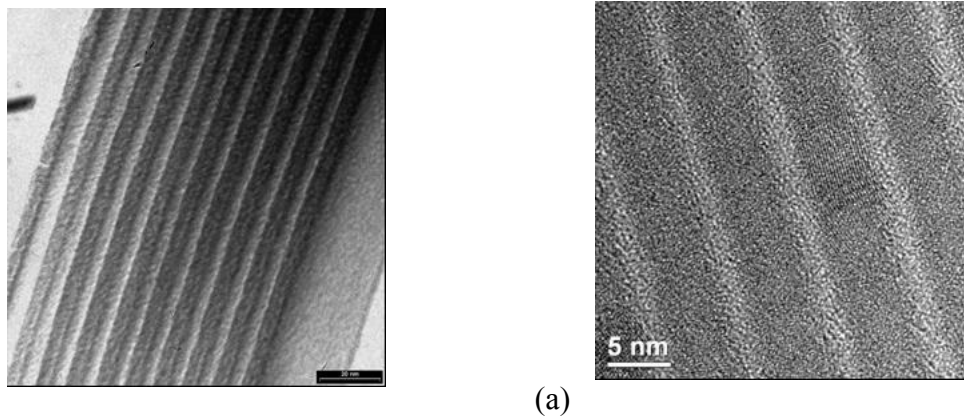


Figure 15: TEM images of SiC/Silicon-rich SiC multilayer (a) as-deposited and (b) annealed at 1100°C for 20 minutes.

Bandgap engineering of silicon nanostructure

Photoluminescence (PL) on the Si QDs in silicon oxide has confirmed that we get a

1.7 eV lowest energy transition from 2 nm quantum dots; effectively a 1.7eV bandgap [6]. They also show that there is a large increase in PL intensity as the QD size decreases, which is consistent with the increase in radiative efficiency with the onset of pseudo-direct band gap behaviour.

We also observed that the photoluminescence peaks from Si QDs in nitride are more blue-shifted than that of Si QD in oxide. Data from other authors are shown in Figure 1, section 2 together with a discussion of the modification of surface QD states by the matrix which leads to varying confined energies.

Tin (Sn) QDs in silicon oxide

The work on Si QDs in dielectric matrices involves a high temperature anneal (except for the in-situ Si QDs in Si₃N₄ work). Furthermore, such technology can only ever increase the band gap of an engineered nanostructure, not decrease it. Hence we are also considering other group IV elements as QDs in a dielectric matrix. Both Sn and Ge are likely to precipitate at lower temperatures in an appropriate analogue material. Also as Sn and Ge also both have lower bulk band gaps, they can produce a QD nanostructure with effective band gap below that of Si. This could be useful for fabrication of a nanostructure cell to stack below a Si cell in a tandem stack.

We are currently concentrating on Sn as it is a much more readily available material than Ge (although their total abundance in the Earth's crust is similar). Although the bulk value of the Sn band gap is lower than that of Si, it increases more rapidly with decreasing size and exceeds that of Si for very small sizes. The electron effective mass of α -Sn is 0.0236 m_0 and its Bohr radius corresponds to 40 nm. Semi-empirical tight binding calculation indicates an effective bandgap of 0.4 eV for 20 nm dots and 2.5 eV for 5 nm dots [35]. Figure 16 shows the theoretical bandgap of Sn nanocrystals due to quantum confinement.

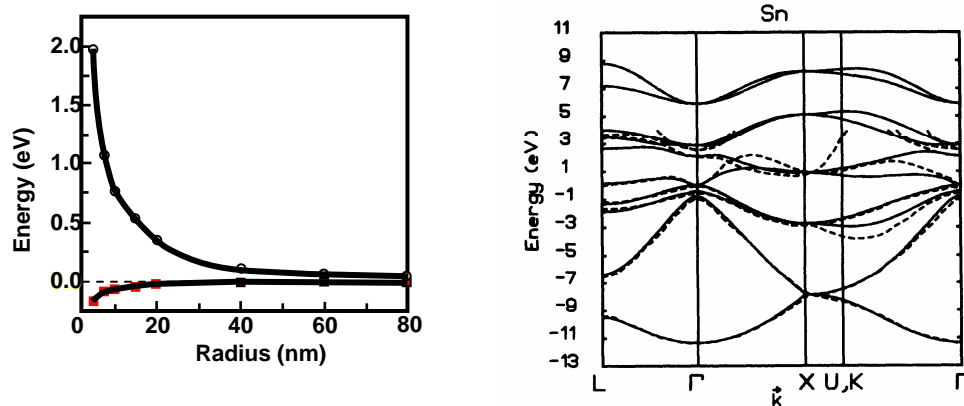


Figure 16: Semi-empirical tight binding calculation of Sn nanocrystals [35] and the α -Sn band structure [36].

Sn has two polymorphic structures: The semi-metallic α -Sn (diamond cubic Sn) and truly metallic β -Sn (double body-centered-tetragonal). α -Sn has conduction band minima at the Γ point below the valence band and is a semi-metal with bandgap of 0.08 eV at 300°K. A phase transition from α -Sn to β -Sn occurs at 13.2°C. [36]

Our first experiments on a Sn nanostructure have involved Sn precipitation from a Sn-rich SiO₂ layer. Whilst this is a more complex system, it is a more direct analogue of our existing technologies and we can build on our existing knowledge of the SiO₂ processing parameters.

The Sn-rich precursor layers were prepared by magnetron co-sputtering of Sn and SiO₂. The Sn content in the Sn-rich SiO₂ film was controlled by changing the RF plasma power, while the power of the DC supply was maintained at 2.5 W. The volume percentage of Sn in the samples was 23% calculated from the sputter rates of Sn and SiO₂. TEM images of an as-deposited sample showed a uniform Sn-rich SiO₂ layer without clear precipitations (not shown). In contrast, Sn atoms precipitated to form nanocrystals in the samples that were annealed after deposition in the vacuum chamber, as shown in Figure 17. The mean diameter of nanocrystals in the middle region increased from about 7.4 nm (400 °C) to 17.2 nm (700 °C).

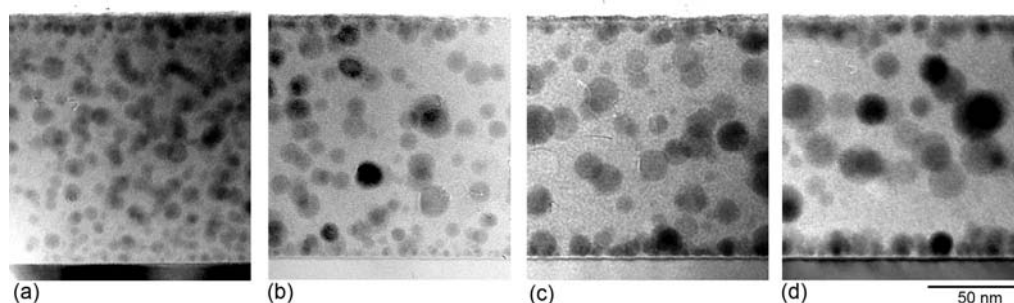


Figure 17: Cross-sectional TEM images of Sn QDs films annealed at (a) 400°C, (b) 500°C, (c) 600°C, and (d) 700°C.

This result suggests that Sn atoms precipitate to small nanoclusters during annealing and aggregate to larger dots by diffusion. At high annealing temperatures, Sn has a high solubility in SiO₂ resulting in fast diffusion and growth processes to form bigger dots.

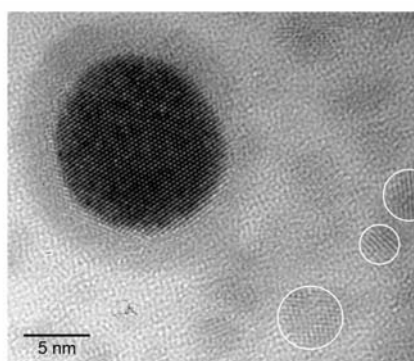


Figure 18: HRTEM plan-view of Sn nanocrystal showing single crystalline structure of β -Sn and Sn oxide nanoclusters circled by white circles.

From HRTEM imaging, we observed that most of the nanocrystals show homogenous lattice fringes, as per the large dot shown in Figure 18, suggesting that the nanocrystals comprise a single crystalline structure. The typical fringe spacings measured from the HRTEM images are 2.9 Å and 2.8 Å, which correspond to the (200) and (101) lattice planes of β -Sn respectively. Some of nanocrystals feature a shell with lower contrast surrounding the crystallized core, which is considered to be Sn oxide (Fig. 2). In addition, we observed small nanocrystals 2.5~5.0 nm in diameter with lower contrast from all vacuum annealed samples. When exposed for a

few minutes to the electron beam in the TEM chamber, these nanocrystals revealed a clear fringe spacing of 3.3 Å as shown by the white circles in Fig. 2, which corresponds to the (110) lattice plane of SnO₂.

With the intention of forming Sn nanocrystals of uniform size, a multilayer structure of Sn-SiO₂ alternating with a stoichiometric SiO₂ layer was deposited. This was annealed at the relatively low temperature of 400 °C for 1 hour in the vacuum chamber. Figure 19 shows a plan-view TEM image of a single layer of Sn QDs embedded in SiO₂. By annealing the sample at 600 °C in N₂, a very uniform size of Sn QDs of 3.5±0.6 nm was obtained. The density of the quantum dots and inter-dot spacing can be readily controlled by changing the Sn content.

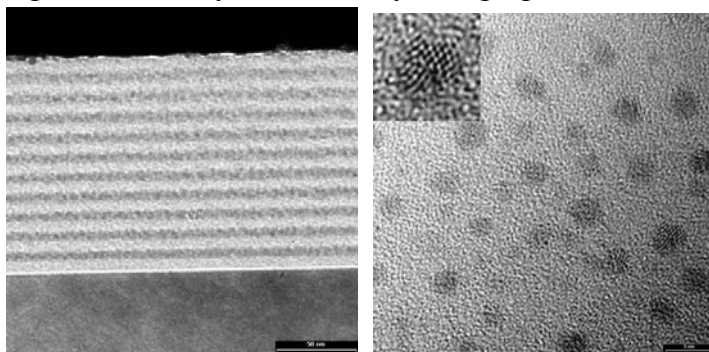


Figure 19: (a) TEM image (cross section) of tin quantum dot layers prepared in an oxide matrix; (b) HRTEM image (plan view) of a single layer of tin quantum dots giving additional information on lateral spacing. Inset: lattice plane image.

Further chemical, structural and optical characterisation is underway along with further investigation of deposition properties and possible photovoltaic application.

Nano-Si containing SiC/Si heterojunction

Silicon nanocrystals (Si-NCs) embedded in a silicon carbide (SiC) matrix (abbreviated Si-NC:SiC) were used to prepare heterojunction (HJ) solar cells to evaluate electrical material quality of the Si-NC:SiC film and its applicability for photovoltaic applications. The HJ cells were fabricated from p-type Si-NC:SiC film on n-type crystalline silicon substrates (Si-NC:SiC/c-Si). Figure 20 shows a schematic of the HJ solar cells. It is not intended that these devices demonstrate enhanced efficiencies – as the Si substrate configuration precludes this - rather they are intended to investigate junction properties with one side of the junction being a very well characterized Si wafer.

The device substrate was *n*-type silicon wafer, (100)-oriented with a resistivity of 2-9 Ωcm. The films were in situ doped with boron via boron-doped SiC and Si targets. The as-deposited film is Si_{1-x}C_x/SiC multiplayer. The thickness of individual layers was 4-10 nm and total thickness was about 150 nm (10 – 20 periods). After annealing at 1100 °C, the Si-NC:SiC film was formed as a emitter. The back and front ohmic contacts were made by evaporating Al. The cell area was 1.0×1.0 cm².

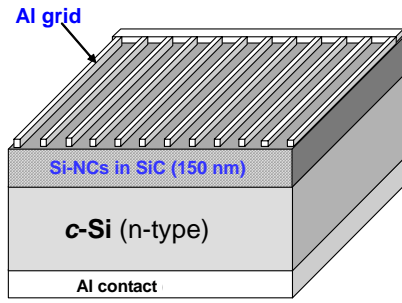


Figure 20: Schematic diagram of cross section of a p-type Si-NC:SiC/n-type *c*-Si heterojunction solar cells.

The electrical and photovoltaic properties of the HJ devices are characterised by illuminated and dark I - V and quantum efficiency measurements. Figure 21 shows dark I - V characteristics of a *p*-type Si-NC:SiC/n-type *c*-Si HJ solar cell measured at room temperature in both polarities. The diode shows a good rectification ratio of 1.0×10^4 at ± 1.0 V. The local ideality factor was 1.24 at $V = 0.1 - 0.5$ V. Figure 22 shows 1-Sun I - V curve of a typical Si-NC:SiC/*c*-Si HJ solar cell measured under the standard AM1.5G spectrum with an illumination level of 100 mW/cm^2 at 298 K. The cell has V_{oc} of 463 mV, J_{sc} of 19 mA/cm^2 , fill factor of 53 %, and conversion efficiency of 4.66 %. The illuminated I - V curve exhibits relatively poor cell performance due to high series resistance ($4.72 \Omega \text{ cm}^2$) and low shunt resistance ($914 \Omega \text{ cm}^2$). Most, if not all, of the absorption in this device will be in the Si wafer and hence not demonstrate absorption in the SiC or QD layers. It should also be noted that a heterojunction can be formed between SiC without nanocrystals and a Si wafer, nonetheless the demonstration of a rectifying heterojunction in these structures is an encouraging step towards a full photovoltaic device.

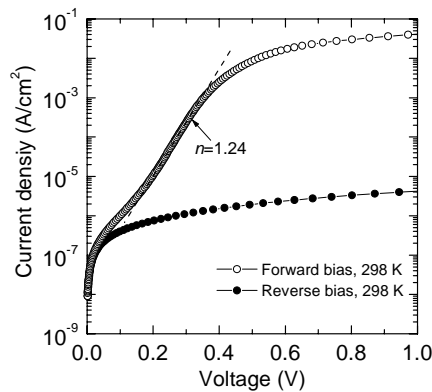


Figure 21: Dark forward and reverse I - V curves of one of the studied Si-NC:SiC/*c*-Si HJ solar cells measured at room temperature.

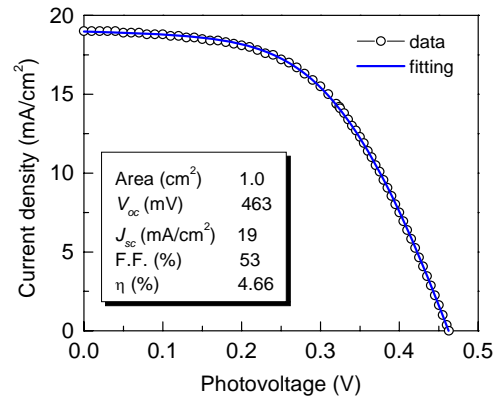


Figure 22: Measured 1-Sun I - V curve (298 K, 100 mW/cm^2) of a typical Si-NC:SiC/*c*-Si HJ solar cell.

Figure 23 shows the hemispherical reflection (R), external quantum efficiency (EQE) and internal quantum efficiency (IQE) of the cell. For the blue wavelength response, the IQE is ~ 35 % at 400 nm. This appears to be higher than that for a conventional *c*-Si homojunction solar cells and this may be due to some contribution to absorption by either the wider band-gap *a*-SiC or possibly the Si-nanocrystals in the SiC. The large J_{sc} difference from the EQE and the IQE is due to a high front surface reflection of the

cells. The relatively poor full-wavelength response of the *IQE* (peak at ~89 %) suggests a large collection loss of photo-generated carrier in the cells, which was caused by more defects at the junction interface due to the different thermal expansion coefficient of these two materials.

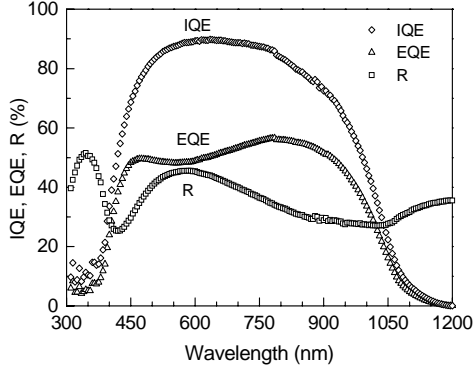


Figure 23: Measured hemispherical reflection (*R*), external quantum efficiency (*EQE*) and internal quantum efficiency (*IQE*) of the cell.

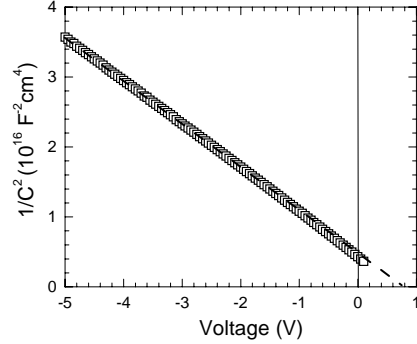


Figure 24: C-V plot of of a Si-NC:SiC/*c*-Si heterojunction.

The C-V plot in Figure 24 shows a good linear relationship over a wide voltage range from -5.0 V to 0.1 V. The built-in potential of the junction deduced from this C-V plot is 0.8 V, which means there is room to improve the device performance.

Although the performance of these preliminary devices need further improvement, this initial study indicates that the Si-NC:SiC films are promising for preparing a homojunction photovoltaic device by p-type and n-type quantum dot materials.

4 Future Plans

Doping in bulk semiconductors is normally considered as continuous throughout an entire volume, however nanocrystals, i.e., quantum dots, often have zero impurity and defect concentrations. If we consider a doped bulk semiconductor, a doping concentration of 10^{18} cm^{-3} is usually considered high. Applying to a spherical quantum dots of 5 nm in size, one quantum dot with a doping density of 10^{18} cm^{-3} has less than one dopant atom on average. Also impurity atoms in quantum dots are excluded from quantum dots onto the particle surface, which is known as a “self purification” during the crystallization [37]. We are investigating the doping issues to fabricate doped quantum dot superlattice p-n junction or p-i-n junction with the superlattice as i-region. A heterojunction of Si quantum dots and crystalline silicon was fabricated and its characteristics are being investigated. The first results are already included in this report and this work will soon deliver more results. Homojunctions of doped p- and n-type silicon QD nanostructures are being tested on silicon, insulator and transparent conducting substrates, with the aim of demonstrating a Si QD cell of V_{oc} greater than 600 mV.

The modeling work using DF-HF computations will build on our results to-date. These underline the importance of investigating the electronic structure of the interface with respect to the various dielectrics (oxides, nitrides, carbides). This work

will be continued in order to achieve conclusive results. Another issue is the evaluation of intrinsic and extrinsic defects. For the latter, one aim will be to find suitable impurities for modulation doping - as frequently used in III-V quantum well superlattices. Such doping has the advantage of leaving the mechanical and electronic structure of the Si QDs unperturbed, although still allowing them to be ionized by carriers from the doped dielectric matrix. This requires impurities which are well above (below) the confined electron (hole) states in the Si QDs in both the dielectric matrix *and* the Si QDs. Such dopants would not be in the energy range of carrier generation and transport and hence they would not alter the electronic structure in terms of QD eigen energy within the QDs and would also not contribute to carrier recombination. [38]

Hence the work in the next period, both in fabrication and modeling, will focus on formation of p-n or p-i-n junctions in the QD nanostructures; and the demonstration of photovoltaic effects.

5 Publications

1. M. A. Green and G. Conibeer, "Nanostructured Silicon-Based Tandem Solar Cells", Stanford Global Climate and Energy Project Symposium, San Francisco, September 2006 (invited).
2. M.A Green, G. Conibeer, D. König, E.-C. Cho, D. Song, Y.-H. Cho, T. Fangsuwannarak, Y. Huang, G. Scardera, E. Pink, S. Huang, C. Jiang, T. Trupke, R. Corkish, T. Puzzer, "Progress with all-Silicon Tandem cells Based on Silicon Quantum Dots in a Dielectric Matrix", Proc. 21st European Photovoltaic Solar Energy Conference, Dresden, Sept 2006, p. 10.
3. M. A. Green, "A New Class Of Semiconductor Using Quantum Confinement Of Silicon In A Dielectric Matrix", Future Trends in Microelectronics Conference, Crete, September, 2006.
4. M. A. Green, "Nanostructure Silicon Quantum Dot Tandem and Hot Carrier Solar Cells", MRS Spring Symposium, San Francisco, April 2006 (invited).
5. G. Conibeer, M.A. Green, R. Corkish, Y.-H. Cho, E.-C. Cho, C.-W. Jiang, T. Fangsuwannarak, E. Pink, Y. Huang, T. Puzzer, T. Trupke, B. Richards, A. Shalav, K.-L. Lin, "Silicon nanostructures for third generation photovoltaic solar cells", Thin Solid Films 511/512 (2006) 654.
6. E.-C. Cho, M. A. Green, R. Corkish, P. Reece, M. Gal and S.-H. Lee "Photoluminescence in crystalline silicon quantum wells", Journal of Applied Physics, 101, 024321 (2007).
7. D. König, M.A. Green, G. Conibeer, Y. Takeda, T. Ito, T. Motohiro, T. Nagashima, Proc. 21st European Photovoltaic Solar Energy Conference, Dresden, Sept 2006, p. 164.
8. T. Fangsuwannarak, G. Conibeer, G. Scardera, E.-C. Cho, E. Pink, Y. Huang and M. A. Green, "Effects of silicon nano-crystallite density on the Raman-scattering spectra of silicon quantum dot superlattices", SPIE 2006, Adelaide, Australia, November 2006.
9. T. Fangsuwannarak, T. Trupke, E. Pink, G. Conibeer, Y. Huang, T. Puzzer and M. A. Green, "Analysis of the effect of Si quantum dot density on the photoluminescence Spectra of Si /SiO₂ quantum dot superlattices", 21st European Photovoltaic Solar Energy Conference, Dresden, Germany, 4-8 September 2006.
10. C. Flynn, D. König, G. Conibeer, "Capacitance-Voltage Characterisation of Silicon Quantum Dot Superlattices for Photovoltaics Applications", Solar 2006 Proceedings - ANZSES 44th Annual Conference, The Australian National University, Canberra, Australia 2006.
11. G. Scardera, T. Puzzer, D. McGrouther, E. Pink, T. Fangsuwannarak, G. Conibeer and M. A. Green, "Investigating Large Area Fabrication of Silicon Quantum Dots in a Nitride Matrix for Photovoltaic Applications", 4th World Conference on Photovoltaic Energy Conversion (WCPEC), Hawaii, USA, 7-12 May 2006.
12. G. Scardera, T. Puzzer, E. Pink, G. Conibeer and M. A. Green, "Effect of Annealing Temperature on the Formation of Silicon Nanocrystals in a Nitride Matrix", SPIE 2006, Adelaide, Australia, November 2006.
13. D. Song, E.-C. Cho, Y. H. Cho, E. Pink, G. Conibeer and M. A. Green, "Effects of Post-Annealing Process on the Structural and Optical Properties of Si-rich SiC Films for Photovoltaic Applications", Solar 2006 Proceedings - ANZSES 44th Annual Conference, The Australian

- National University, Canberra, Australia, 2006.
14. C-W. Jiang and M. A. Green, "Silicon Quantum Dot Superlattices: Modelling of Energy Bands, Densities of States and Mobilities for Silicon Tandem Solar Cell Applications", *Journal Applied Physics*, Vol. 99, 114902, 2006.
 15. Lap Van Dao, Jeff Davis, and Peter Hannaford, Young-Hyun Cho, Martin A. Green, and Eun-Chel Cho, *Appl. Phys. Lett.* 90, 081105 (2007).

6 Contacts

Prof. Martin Green: m.green@unsw.edu.au
 Dr. Gavin Conibeer: g.conibeer@unsw.edu.au

7 References

- [1] P.J. Walters, G.I. Bourianoff, H.A. Atwater, *Nat. Mater.* 4 (2005) 143.
- [2] L. Pavesi, L. Dal Negro, C. Mazzoleni, G. Franzo, F. Priolo, *Nature* 408 (2000) 440.
- [3] M. Cazzanelli, D. Navarro-Urriós, F. Riboli, N. Dalbosso, L. Pavesi, J. Heitmann, L.X. Yi, R. Scholz, M. Zacharias, U. Gösele, *J. Appl. Phys.* 96 (2004) 3164.
- [4] M.A Green, E.-C. Cho, Y.-H. Cho, E. Pink, T. Trupke, K.-L. Lin, T. Fangsuwannarak, T. Puzzer, G. Conibeer, R. Corkish, *Proceeding of 20th European Photovoltaic Solar Energy Conference*, Barcelona, Spain, June 6-10, 2005, p. 3.
- [5] G. Conibeer, M.A. Green, R. Corkish, Y.-H. Cho, E.-C. Cho, C.-W. Jiang, T. Fangsuwannarak, E. Pink, Y. Huang, T. Puzzer, T. Trupke, B. Richards, A. Shalav, K.-L. Lin, *Thin Solid Films* 511/512 (2006) 654.
- [6] E.-C. Cho, Y.H. Cho, T. Trupke, R. Corkish, G. Conibeer and M.A. Green, *Proc. 19th European Photovoltaic Solar Energy Conference*, Paris, (June 2004), p. 235.
- [7] F. Meillaud, A. Shah, C. Droz, E. Vallat-Sauvain, C. Miazza, *Sol. Energy Mater. Sol. Cells* 90, 29522 (2006).
- [8] M. Zacharias, J. Heitmann, R. Scholz, U. Kahler, M. Schmidt, *Appl. Phys. Lett.* 80 (2002) 661.
- [9] T. Argyurov, T. Mchedlidze, M. Kittler, R. Rölver, B. Berghoff, M. Först, B. Spangenberg, *Appl. Phys. Lett.* 89 (2006) 053111.
- [10] T.-W. Kim, C.-H. Cho, B.-H. Kim, S.-J. Park, *Appl. Phys. Lett.* 88 (2006) 123102.
- [11] Y.-H. Cho, E.-C. Cho, Y. Huang, C.-W. Jiang, G. Conibeer, M.A. Green, *Proceeding of 20th European Photovoltaic Solar Energy Conference*, Barcelona, Spain, June 6-10, 2005, p.47.
- [12] Y. Kurokawa, S. Miyajima, A. Yamada and M. Konagai, *Jpn. J. Appl. Phys.* 45, L1064 (2006).
- [13] S. Ossicini, F. Iori, E. Degoli, E. Luppi, R. Magri, R. Poli, G. Cantele, F. Trani, and D. Ninno, *IEEE J. of Selected Topics in Quantum Electronics* 12, 1585 (2006).
- [14] G. Polisski, D. Kovalev, G. Dollinger, T. Sulima, and F. Koch, *Physica B* 273, 951 (1999).
- [15] Y. Kanemitsu, *J. Luminescence* 70, 333 (1996).
- [16] H. Takagi, H. Ogawa, Y. Yamazaki, A. Ishizaki, and T. Nakagiri, *Appl. Phys. Lett.* 56, 2379 (1990).
- [17] S. Takeoka, M. Fujii and S. Hayashi, *Phys. Rev. B* 62, 16820 (2000).
- [18] T. Y. Kim, N. M. Park, K. H. Kim, G. Y. Sung, Y. W. Ok, T. Y. Seong, and C. J. Choi, *Appl. Phys. Lett.* 85, 5355 (2004).
- [19] A. Puzder, A.J. Williamson, J.C. Grosman, G. Galli, *J. Chem. Phys.* 117, 6721 (2002).
- [20] M-S. Yang, K-S, Cho, J-H, Jhe, S-Y. Seo, J.H. Shin, *Appl. Phys. Lett.* 85, 3408 (2004).
- [21] D. König, M.A. Green, G. Conibeer, Y. Takeda, T. Ito, T. Motohiro, T. Nagashima, *Proc. 21st European Photovoltaic Solar Energy Conference*, Dresden, Sept 2006, p. 164.
- [22] S. Ogut, J.R. Chelikowsky, S.G. Luoie, *Phys. Rev. Lett.* 79, 1770 (1997).
- [23] L.E.Ramos, J. Furthmüller, F. Bechstedt, *Effect of oxidation on Si nanocrystallites*, *Phys. Rev B* 70, 033311 (2004).
- [24] M. Luppi, S. Ossinici, *Ab-initio study on oxidized silicon clusters and silicon nanocrystals embedded in SiO2: Beyond the quantum confinement effect*, *Phys. Rev. B* 71, 035340 (2005)
- [25] F. Reboredo, G. Galli, *Theory of Alkyl Terminated Silicon Quantum Dots*, *J. Phys. Chem. B*, UCRL-JRNL-207526 (2004)
- [26] Y. Fan, X.L. Wu and Paul K. Chu, *Progress in Materials Science* 51, 983 (2006).
- [27] M.A.Green, "Third Generation Photovoltaics", Springer, 2003.

-
- [28] E.-C. Cho, M.A. Green, J. Xia, R. Corkish, P. Reece and M. Gal, *Appl. Phys. Lett.* 84 (2004), p. 2286.
- [29] K. Boer, "Survey of Semiconductor Physics", van Nostrand Reinhold, 1990.
- [30] C.W. Jiang, M.A. Green, *J. Appl. Phys.* 99, 114903 (2006).
- [31] <http://www.gaussian.com>
- [32] Kirkland, E. J., "Advanced Computing in Electron Microscopy" Plenum Press, New York (1998).
- [33] Wolfram Research, Inc., *Mathematica*, Version 5.2, Champaign, IL (2005).
- [34] V. Domnich, Y. Gogotsi, and S. Dub, *Appl. Phys. Lett.* 76 (2000) 2214.
- [35] R. Ragan, "Direct energy band gap group IV alloys and nanostructures." PhD theseis (Caltech, 2002).
- [36] D. W. Jenkins and J. D. Dow, *Phys. Rev. B* 36 7994 (1987).
- [37] S. C. Erwin, L. J. Zu, M. I. Haftel, A. L. Efros, T. A. Kennedy, D. J. Norris, *Nature* 436, 91 (2005).
- [38] S. Ossini, F. Iori, E. Degoli, E. Luppi, R. Magri, R. Poli, G. Cantele, F. Trani, D. Ninno, Understanding Doping IN Silicon Nanostructures, *IEEE J. Sel. Top. Quant. Electron.* 12, 1586 (2006).